Preprints of the 19th World Congress
The International Federation of Automatic Control
Cape Town, South Africa. August 24-29, 2014

Modelling and Controller Design of Resonant Thermoacoustic Solar AC Power Generators

Boe-Shong Hong*. Chia-Yu Chou

Department of Mechanical Engineering, National Chung Cheng University, Chia-Yi 621, Taiwan (Tel: 886-5-2720411 ext. 33321; e-mail: imehbs@ccu.edu.tw).

Abstract: This paper installs resonant controller on thermoacoustic engines to increase their power ratings enormously. The thermoacoustic engine under design for solar power is assembled by alternative current generator, Rijke tube, and switching radiation-to-heatflux actuator. A limit-cycle generator is programmed into a microcontroller embedded with a DSP engine, which temporally keeps the switching frequency of the photo valve on one of resonant frequencies to pump up vibration power. Furthermore, the Rijke tube is longitudinally shaped to make power transmission more efficient. Through the following developments, we arrive at a sound design: (1) Synthesis of limit-cycle generators with online adjustable frequencies for power-rating boost; (2) Analytic Rayleigh Dynamics to shape the Rijke tube for efficient power-transmission; (3) 2D transfer-function to transform the overall design into feedback systems for optimizing impedance matching of Rijke tube and AC power generator and assessing resonant frequencies; and (4) Conservation law of Rayleigh storage to Figure out engine cycles that provide fundamental principles to thermoacoustic engines design.

Keywords: Rayleigh criterion, nD transfer function models, Least-action principle, Limit-cycle generator.

1. INTRODUCTION

Of facilities generating electricity from sunlight, thermoacoustic engine under resonant control is of much less ratio of manufacturing cost to power rating than pure photovoltaics, solar-thermal devices, and other heat engines. Its extremely simple mechanism enables us to build solar power plants in poor lands and home rooftops at affordable prices. Besides, thermoacoustic engines can have power efficiency even better than Carnot cycle efficiency that merely exists in an ideal heat engine.

A thermoacoustic engine generates, transferred, and amplifies wave motions in fast-time scale for power generation. In passive designs, say in Shen, He, Li, Zhang, and Liu (2009); Wu, Dai, Man, and Luo (2012), heating-cooling and contraction-expansion processes occur in thermo-fluid perturbation, behaving like vibration Carnot cycles. A vibration Carnot engine is made of three main modules: thermal storage being the source of fast-time heat-flux, Rijke tube for transformation of thermal power to acoustic power, and AC mechatronic load to transform acoustic power to mechanical power to electricity to be stored. The feedback coupling between the heat-transfer dynamics in thermal storage and the acoustic dynamics in Rijke tube evolves to sustained limit-cycle oscillation at some frequency. The construction of impedance at this frequency becomes the design tool on those three modules (Smoker, Nouh, Aldraihem, & Baz, 2012; Yu & Jaworski, 2010; Yu, Jaworski, & Backhaus, 2012).

To increase power rating, we install crystal liquid photo valve, which consumes very little power, on the head end of Rijke tube, as shown in Fig. 1. It is actively controlled to switch at resonant frequencies of thermoacoustic vibration. At the engine's head Rijke tube takes fast-time heat-flux, directly or indirectly from the sunlight, giving rise to entropy rate that changes the fluid density there, which in turns initiates acoustic velocity. Therein, the heat-flux excitation expanding and contracting the fluid acts as a source of acoustic wave that rides on Rijke-tube media and arrives at the load end to push and pull the piston, generating mechanical work. Inside the controller, a limit-cycle generator online keeps the switching frequency of photo valve to one of natural frequencies, which prompts standing waves up to resonance and thus increases mechanical power enormously.

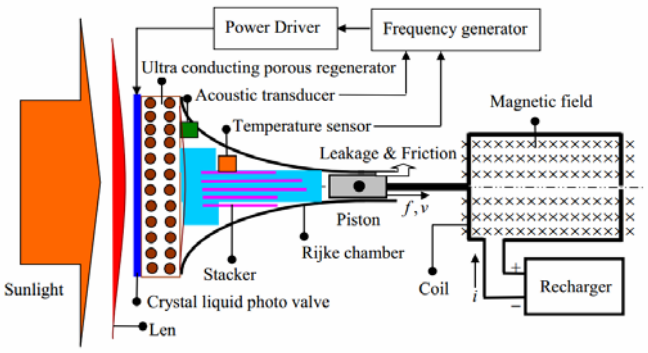

Fig. 1. Overall design of resonant thermoacoustic engines.

The dynamics inside the Rijke tubes of thermoacoustic engine has been intensively studied in recent years, for examples in Hong, Chou, and Lin (2013); Jung and Matveev (2010); Matveev and Jung (2011); Zhao (2013); Zhao and

Chew (2012), based on impedance analysis, computational fluid dynamics or nD transfer function. In fact, such dynamics is nearly identical to that in the field of combustion instabilities, for examples in Hong and Lin (2007); Hong, Ray, and Yang (2002); Matveev and Culick (2003); Sujith, Waldherr, and Zinn (1995); Zhao (2012). Both thermoacoustic engines and combustion instabilities are mainly concerned with the process how heat perturbation excites acoustic motions, known as *Rayleigh Criterion* (Culick, 1987; Durox, Schuller, Noiray, Birbaud, & Candel, 2009; Ferreira & Carvalho, 1997; Hong et al., 2012; Nicoud & Poinsot, 2005). In this paper, the Rayleigh criterion is further formulated into the principle of least action, named here by *Analytic Rayleigh Dynamics*. It is then employed to derive the wave equation governing energy transfer along Rijke tubes of spatially variant cross-section areas. As the cross-section of Rijke rube is narrowed from head to tail, power is transmitted from the head end with larger pressure and tiny velocity to the load end with required velocity and piston stroke. Due to high-pressure AC power transmission, this significantly reduces the viscosity effect inside the Rijke tube and thus increases energy efficiency.

For control modelling, the wave equation above in conjunction with inhomogeneous boundary conditions of Rijke tube is then transformed into a single spatiotemporal transfer function, which is an extended application of the functional tool known as nD transfer function models (Hong, 2010; Hong, Su, Chou, & Hung, 2011; Rabenstein, 1999; Rabenstein & Trautmann, 2002, 2003). Therein the inhomogeneous boundary conditions arise from the von Neumann source of heat-flux at head end and the Robin source of piston-speed at tail end, both of which are transformed into Dirac distribution by way of 2D transfer-function. This renders the capability of representing the dynamics coupling between Rijke tube and AC mechanical load into feedback interconnection, and thus of transforming the engine design into synthesis of feedback systems. Based on this feedback realization, digital signal processing can be programmed to numerically assess in frequency domain the power rating and resonant frequencies.

For power amplification, the filtered Van der Pol oscillator is implemented into a DSP-controller that provides sinusoidal control signals and is capable of modulating frequency in a real-time fashion. Its dynamics is transformed into iterated computation of addition and multiplication performed by the DSP engine inside. This kind of DSP-based implementation (Hong, Lin, & Su, 2009; Tassart, 2013; Wang, Yang, & Xu, 2013) is in line with the function of the DSP engine that is a master of fast calculation of addition and multiplication of floating numbers. Microcontrollers are really needed in practice for frequency synthesizers, since analogue circuits lack communication ports, crystal oscillators have no reliable low-frequency outputs, and general-purpose computers transport signals to peripheral devices very slowly. Furthermore, DSP-based linear oscillators are not candidates, since they produce in the long run no sustained oscillations.

For the time being, there are two popular frequency synthesizers in industry: one is by data scheduling (Yeary, Fink, Beck, Guidry, & Burns, 2004) and the other is by online sinusoidal function (de Caro, Napoli, & Strollo, 2004; Madheswaran & Menakadevi, 2003), both of which are widely used in wireless communication. In the type of data scheduling, the working chip stores a table of data in code space that digitally shape a sinusoidal function. The targeted frequency is determined by the number of times of fetching the whole table per second at fixed instruction clock, which is adjustable by the number of entries to be fetched in the entire table. This requires large size of ROM for long table and produces wide frequency-span for radio modulation. Such size of ROM is usually unavailable in DSP-controllers, and building special ICs for this purpose prevails (de Caro, Napoli, & Strollo, 2004; Madheswaran & Menakadevi, 2003). One characteristic of data scheduling for frequency synthesizer is low frequency-resolution, since the number of entries being fetched is always an integer. This situation is worse at lower frequency-range. It prevents this method from being applied to resonant control of thermoacoustic engines, wherein small change of exciting frequency away from resonant frequencies will seriously retard the amplitude of pressure in Bode plot. On the other hand, with the limit-cycle approach as developed by this paper, the frequency resolution can be pushed to the maximum allowed by hardware, which is usually more than 16 mega.

In the type of on-line sinusoidal function, the working chip has to compute sinusoidal function one time within each sampling periods, wherein the sinusoidal function is approximated by Taylor-series expansion (de Caro et al., 2004) or by other complex algebra. Such a high computation burden is beyond the capability of DSP-controllers, and often requires FPGA chips. However, we really need DSP-controllers for resonant control of thermoacoustic engines, since in the chip are not just frequency synthesizer but also on-line window Fourier transform for detecting shifting of resonant frequencies, and colour and white noises filters to remove sensing contamination. All of these modules are through DSP-based implementation. Otherwise, a special IC or a single-task FPGA is unable to be integrated into other modules to fulfil control purpose. Moreover, there is usually a variety of peripherals in DSP-controllers served for control purpose. For example, almost every Microchip dsPIC has analogue-to-digital (A/D) and pulse-width modulation (PWM) peripherals, for inputting analogue signals from sensors and outputting PWM signals to switching power converters.

2. ANALYTIC RAYLEIGH DYNAMICS

According to the reference (Hong et al., 2013), the thermoacoustic dynamics inside a Rijke chamber can be formulated to be:

$$\frac{\partial^2 \psi}{\partial t^2} - \frac{1}{R_a} \nabla \cdot (\kappa R_a \nabla \psi) = (\gamma - 1) Q \quad . \tag{1}$$

Therein, Q stands for fast-time heat-rate, and ψ for thermoacoustic momentum defined by the temporal integration of acoustic pressure p, that is,

$$p = \frac{\partial \psi}{\partial t}\ ;\ \widetilde{\rho} u = -\nabla \psi\ , \tag{2}$$

where $\widetilde{\rho}$ stands for mean density and u for acoustic velocity. As to parameters in Eq. (1), $R_a \equiv (\widetilde{p}/\widetilde{p}_0)^{(1-\gamma)/\gamma}$ is the dimensionless Rayleigh factor, $\kappa = \gamma R \widetilde{T}$ denotes the compressibility, and $\widetilde{p}_0$ is chosen as the environmental pressure.

To quantify the Rayleigh criterion, define two internal scalars: *Rayleigh's Kinetics* K_R, *Rayleigh's Potential* P_R and one line integral *Rayleigh's Work* W_R respectively by

$$\begin{aligned} 2K_R &\equiv \int_{\Omega} R_a (\frac{\partial \psi}{\partial t})^2 dV, \\ 2P_R &\equiv \int_{\Omega} \kappa R_a \left|\nabla \psi\right|^2 dV, \\ dW_R &\equiv \int_{\Omega} d\psi \cdot R_a (\gamma - 1) Q\, dV. \end{aligned} \tag{3}$$

Then, the least-action principle of the Rayleigh criterion becomes

$$0 = \int_{t_1}^{t_2} \boldsymbol{\delta} K_R - \boldsymbol{\delta} P_R + \boldsymbol{\delta} W_R \, dt\ , \tag{4}$$

with respect to the variation of *Rayleigh's displacement* $\boldsymbol{\delta}\psi$, where $\boldsymbol{\delta}$ represents the functional variation. It can be verified that calculus of variation upon Eq. (4) leads to the wave equation of Eq. (1), named here by *Analytic Rayleigh Dynamics*. Fig. 1 shows the thermoacoustic engine under design. We apply the analytic Rayleigh dynamics to derive longitudinal waves in the Rijke tube with non-uniform temperature and cross-section areas.

The heat-flux excitation q (W/m^2) on the head end ($x = 0^-$) activating thermoacoustic process inside the Rijke chamber is equivalent to a pointed heat generation $q\delta(x)$ between $x = 0^-$ and $x = 0^+$ with heat isolation at $x = 0^-$, based on the localization of energy conservation. Here δ is the Dirac delta distribution. With Eq, (3), the Rijke tube stores Rayleigh's Kinetics K_R and Rayleigh's Potential P_R being, respectively,

$$2K_R \equiv \int_0^{\ell} R_a \dot{\psi}^2 A\, dx \ \text{ and } \ 2P_R \equiv \int_0^{\ell} \kappa R_a \psi'^2 A\, dx\ , \tag{5}$$

where A stands for the cross-section area of the Rijke tube that is spatially variant. The Lagrange formulation of the least-action principle of Eq. (4) upon Eq. (5) yields the following longitudinal wave equation:

$$\frac{\partial^2 \psi}{\partial t^2} - \frac{1}{R_a A}\frac{\partial}{\partial x}(\kappa R_a A \frac{\partial \psi}{\partial x}) = (\gamma - 1) q \delta(x) \ \text{ in } [0, \ell)\ , \tag{6}$$

in addition to piston vibration at $x = \ell$. Since the reference pressure $\widetilde{p}_0$ has been chosen as the environmental pressure, the Rayleigh factors on both boundaries are of unity, i.e. $R_a(0) = R_a(\ell) = 1$.

Equation (6) reveals thermoacoustic process happened on the head end between $x = 0^-$ and $x = 0^+$. The hyperbolic nature of Eq. (6) has signified that the acoustic pressure p in Rijke tube is spatially continuous at $x = 0$, i.e. there is no pressure jump from $x = 0^-$ to $x = 0^+$. Thus, the integration of Eq. (6) between $x = 0^-$ and $x = 0^+$ yields the left boundary condition to be

$$C_p \widetilde{T} \psi' = -q\ , \text{ at } x = 0^+\ , \tag{7}$$

where C_p stands for the constant-pressure heat capacitance, $C_p = R\gamma/(\gamma - 1)$. Based on the definition in Eq. (2), Eq. (7) can be rephrased by

$$u = \frac{\gamma - 1}{\gamma}\frac{q}{\widetilde{p}_0} \ \text{ at } \ x = 0^+\ . \tag{8}$$

Equation (8) further reveals that the heat-flux q initiates an acoustic velocity on the left boundary, but keeps the acoustic pressure continuous on the boundary.

The dynamic process on the head end as indicated by Eq. (8) can be realized by tracing back as follows. In between $x = 0^-$ and $x = 0^+$ the heat-flux excitation q gives rise to entropy rate $\dot{s}$ that changes the fluid density, which in turns initiates acoustic velocity. That is, the heat-flux excitation expanding and contracting in fast-time scale the fluid on the boundary $x = 0$ acts as a source of acoustic wave. The acoustic wave rides on Rijke tube media and arrives at the load end at $x = \ell$ to push and pull the piston, and then reflects to eventually be standing waves.

As for the boundary condition at the load end, it is nominally taken to be

$$\psi' = -\widetilde{\rho} v\ , \text{ at } x = \ell^-\ ,$$

where v stands for the piston speed, with the assumption that the acoustic pressure is continuous at $x = \ell^-$ and there is no heat-flux excitation at $x = \ell^+$, If we take flow leakage into consideration, the right boundary condition belongs empirically to the Robin type:

$$\alpha\psi + \beta\psi' = -\widetilde{\rho} v\ , \text{ at } x = \ell^-\ , \tag{9}$$

where $\alpha + \beta = 1$, $\alpha > 0$, $\beta > 0$. Here the *leakage factor* β indicates the ratio of closed area to open area on the load-end boundary, which is to be identified in real design. For succinct notation, $\psi(x,t)$ may appear as $\psi_x(t)$ somewhere in the sequel and similarly to other variables.

3. CONTROL MODELLING

Consequently, the engine dynamics becomes the feedback interconnection of

$$\frac{\partial^2 \psi}{\partial t^2} - \frac{1}{R_a A}\frac{\partial}{\partial x}(\kappa R_a A \frac{\partial \psi}{\partial x}) = 0\ , \text{ in } (0, \ell)\ ; \tag{10}$$

$$C_p \widetilde{T} \psi' = -q\ , \text{ at } x = 0\ ; \text{ and} \tag{11}$$

$\alpha\psi + \beta\psi' = -\tilde{p}v$, at $x = \ell$ ($\alpha + \beta = 1$, $\alpha > 0$, $\beta > 0$), (12)

and the dynamics of alternative current generator. The wave dynamics of Eqs. (10)-(12) involves the elastic stiffness operator $\mathcal{K}$:

$$\mathcal{K}\phi = -\frac{1}{R_a A}\frac{\partial}{\partial x}(\kappa R_a A \frac{\partial \phi}{\partial x}), \quad (13)$$

the domain of which is

$$D(\mathcal{K}) \equiv \{\phi : \phi' = 0 \text{ at } x = 0;\ \alpha\phi + \beta\phi' = 0 \text{ at } x = \ell\}, \quad (14)$$

where $\alpha + \beta = 1$, $\alpha > 0$, and $\beta > 0$.

Based on Sturm-Liouville theory, the stiffness operator $\mathcal{K}$ is self-adjoint and positive-definite under the inner-product:

$$\langle \varphi, \phi \rangle \equiv \int_0^\ell R_a(x) A(x) \phi^*(x) \varphi(x) dx. \quad (15)$$

Denote by Λ the eigenvalues set of the stiffness operator $\mathcal{K}$, corresponding to the eigenfunctions set $\Phi \equiv \{\phi_\lambda\}_{\lambda\in\Lambda}$, i.e.

$\mathcal{K}\phi_\lambda = \lambda\phi_\lambda$ in $[0, \ell]$, $\phi_\lambda \in D(\mathrm{K})$ for $\forall\lambda \in \Lambda$.

Accompanied by $\mathcal{K}$'s self-adjointness is that its eigenfunctions set Φ is real and orthonormal, and followed by $\mathcal{K}$'s positive-definiteness is that all of its eigenvalues are positive, $\lambda > 0$ for $\forall\lambda \in \Lambda$. Moreover, the countable eigenfunctions set Φ is a complete basis of $L_2([0, \ell])$, which follows that the inverse of $\mathcal{K}$ is a bounded operator and closed in the Banach space $L_2[0, \ell]$.

With respect to the eigenfunctions set Φ and the inner-product of Eq. (15), a 2D transform $\mathcal{H}$, named by *Laplace-Galerkin transform*, is then defined by the composite of Laplace transform and Galerkin transform $\mathcal{H} = \mathcal{L}\mathcal{G} = \mathcal{G}\mathcal{L}$, i.e.

$$F(\lambda, s) \equiv \mathcal{H}[f(x,t)] = \int_{t=0^-}^{\infty}\int_{x=0}^{x=\ell} e^{-st} R_a(x) A(x) \phi_\lambda(x) f(x,t) dx dt, \quad (16)$$

to describe f's modal decomposition in the Laplace domain. Accordingly, the inverse Laplace-Galerkin transform is the composite of the inverses of those two 1D transforms, i.e. $\mathcal{H}^{-1} = \mathcal{G}^{-1}\mathcal{L}^{-1} = \mathcal{L}^{-1}\mathcal{G}^{-1}$. Explicitly,

$$f(x,t) \equiv \mathcal{H}^{-1}[F(\lambda,s)] = \frac{1}{2\pi j}\sum_{\lambda\in\Lambda}\phi_\lambda(x)\int_\Gamma e^{ts} F(\lambda,s) ds. \quad (17)$$

At the load end $x = \ell$, substitution of $\alpha\phi_\lambda + \beta\phi_\lambda' = 0$ for Eq. (12)$\times(-\phi_\lambda)$ yields

$$(\psi\phi_\lambda' - \phi_\lambda\psi') = (\phi_\lambda / \beta)\tilde{p}v \text{ at } x = \ell, \quad (18)$$

and the integration by parts yields

$$\int_0^\ell -\frac{\partial}{\partial x}(\kappa R_a A \frac{\partial \psi}{\partial x})\cdot\phi_\lambda\, dx$$
$$= \int_0^\ell -\frac{\partial}{\partial x}(\kappa R_a A \frac{\partial \phi_\lambda}{\partial x})\cdot\psi\, dx + \kappa A\psi'\phi_\lambda\big|_{x=0} + \kappa A(\psi\phi_\lambda' - \phi_\lambda\psi')\big|_{x=\ell}$$

Based on Eq. (10) and (18), the above equation becomes

$$\int_0^\ell -\frac{\partial}{\partial x}(\kappa R_a A \frac{\partial \psi}{\partial x})\cdot\phi_\lambda\, dx = \lambda\langle\psi, \phi_\lambda\rangle - (\gamma - 1) q A_0 \cdot \phi_\lambda(0) + \beta^{-1}\gamma\tilde{p}_0 A_\ell v \cdot \phi_\lambda(\ell), \quad (19)$$

where $R_a(0) = R_a(\ell) = 1$. With Eq. (19), performing Laplace-Galerkin transform $\mathcal{H}$ on Eq. (10) yields

$$(s^2 + \lambda)\Psi(\lambda, s) = (\gamma - 1) A_0 \phi_\lambda(0)\cdot\hat{q}(s) - \tilde{p}_0 A_\ell \beta^{-1}\gamma\phi_\lambda(\ell)\cdot\hat{v}(s), \quad (20)$$

where $\Psi(\lambda, s) \equiv \mathcal{H}[\psi(x,t)]$, $\hat{q}(s) \equiv \mathcal{L}[q(t)]$, and $\hat{v}(s) \equiv \mathcal{L}[v(t)]$. The 2D transfer-function of Eqs. (10)-(12) is thus obtained to be

$$\Psi(\lambda, s) = (\gamma - 1) A_0 \frac{\phi_\lambda(0)\hat{q}(s)}{s^2 + \lambda} - \tilde{p}_0 A_\ell \beta^{-1}\gamma \frac{\phi_\lambda(\ell)\hat{v}(s)}{s^2 + \lambda}, \quad (21)$$

feedback-coupled with the dynamics of alternative current generator. Inversely, performing the inverse Laplace-Galerkin transform $\mathcal{H}^{-1}$ on the spatiotemporal transfer-function of Eq. (21) yields

$$\frac{\partial^2\psi}{\partial t^2} - \frac{1}{R_a A}\frac{\partial}{\partial x}(\kappa R_a A \frac{\partial \psi}{\partial x}) = (\gamma - 1) q(t)\delta(x) - \tilde{p}_0\beta^{-1}\gamma v(t)\delta(x - \ell), \quad (22)$$

with homogeneous boundary conditions:

$$\psi'(0) = 0 \text{ and } \alpha\psi(\ell) + \beta\psi'(\ell) = 0. \quad (23)$$

That is, the wave equation of Rijke tube in Eqs. (10)-(12) is mathematically identical to Eqs. (22)-(23).

In this way, 2D transfer-function of Eq. (21) enables us to realize inhomogeneous boundary conditions as internal sources in conjunction with boundary homogeneity. This represents the engine dynamics as a feedback-interconnection of the chamber dynamics and the dynamics of alternative current generator, as shown in Fig. 2, which transforms the overall design into analysis and synthesis of feedback systems. The feedback-coupled transfer-functions can be straightforwardly realized in Bode plot for assessment of power rating and resonant frequencies.

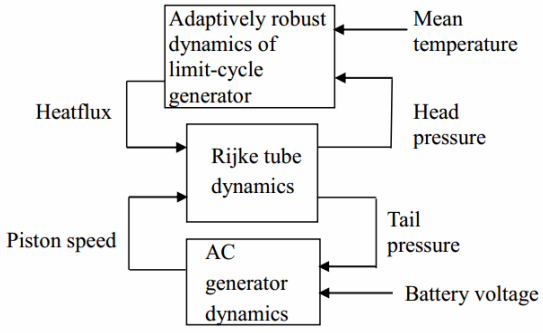

Fig. 2. Feedback-interconnection representation.

4. CONTROLLER DESIGN

In the design of active thermoacoustic engines as sketched in Fig. 1, the feedback control online keeps the switching frequency of radiation-to-heatflux actuator on one of resonant frequencies, which prompts standing waves up to resonance and thus increase mechanical power enormously. Therefore a

limit-cycle generator is programmed into a microcontroller embedded with a DSP engine (dubbed DSP-controller), frequencies of which are adjustable in a real-time fashion. Here we generalize the Van der Po oscillator as the nominated limit-cycle generator.

The Van der Pol oscillator is a non-conservative oscillator with non-linear damping, which evolves in time according to the second order differential equation. Let us consider a more general class of Van der Pol oscillators as

$$\ddot{y} + \mu(y^2 - \frac{a^2}{4})\dot{y} + \omega^2 y = 0\ ;\ \mu > 0\,, \tag{24}$$

where y is the output, and three parameters- a, ω and μ are to be adjusted. The dynamics of Eq. (24) generates a sustained oscillation with amplitude a and angular frequency ω in steady state and the transience period is getting shorter along with increasing value of μ. In the sequel, let us apply *Dynamical Eigenvalue* to approach this claim.

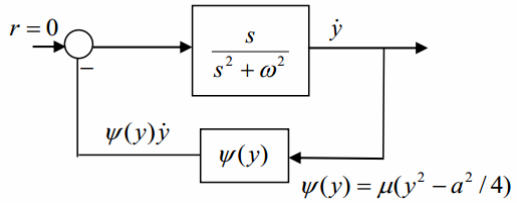

Fig. 3-1. Internal coupling representation of Van del Pol.

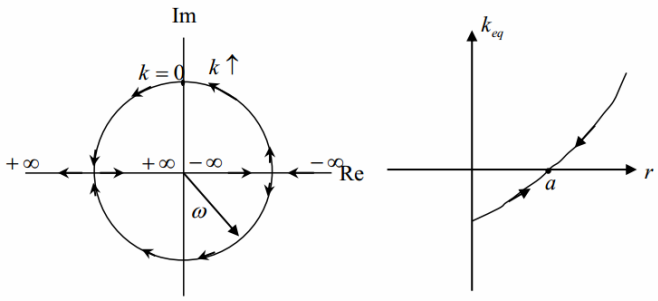

Fig. 3-2. Root Locus and Equivalent Gain

Fig. 3. Synthesis of Van der Pol limit-cycle generators.

Equation (24) can be interpreted by feedback connection as plotted in Fig. 3-1. Therein the nonlinearity $\psi(y)$ is memory-free and thus can be represented as an equivalent gain over each cycle of vibration. Usually, *Describing Function* is used to obtain the equivalent gain k_{eq} of $\psi(y)$ as follows. Let $y = r\sin\omega t$; $\dot{y} = r\omega\cos\omega t$, the output of ψ becomes

$$\psi(y)\dot{y} = \mu r\omega\cos\omega t(r^2\sin^2\omega t - \frac{a^2}{4})$$
$$\equiv a_0 + a_1\cos\omega t + a_2\cos\omega t + \cdots$$

Accordingly, the equivalent gain k_{eq} of the hard-nonlinearity ψ is

$$k_{eq}(r,\omega) = \frac{a_1}{r\omega}\,.$$

Explicitly,

$$k_{eq} = \mu\int_{-\pi/\omega}^{\pi/\omega}(r^2\sin^2\omega t\cos^2\omega t - \frac{a^2}{4}\cos^2\omega t)\,dt = \frac{1}{4}\mu(r^2 - a^2)$$

As predicted, it ought not to dependent on the oscillation frequency ω, since the nonlinearity ψ is memory-free.

In Fig. 3-2 is plotted the Root Locus of $1 + kG(s) = 0;\ G(s) = s/(s^2 + \omega^2)$ and the equivalent gain k_{eq} versus the oscillation amplitude r. Suppose the initial amplitude is larger than a, the closed-loop eigenvalues start running at West Gauss, and hence the amplitude r begins to decrease, which in turn reduces the equivalent gain k_{eq} until the eigenvalues move to East Gauss. However, eigenvalues being at East Gauss increases the amplitude r, and at the same time increases k_{eq}, which moves eigenvalues toward West. As a result, eigenvalues must asymptotically stop at the equilibrium on the imaginary axis corresponding to $k_{eq} = 0$. This implies the steady-state exhibits in sustained oscillation with the amplitude a and angular frequency ω. Suppose the initial amplitude is smaller than a, by the same analysis, the close-loop eigenvalues evolve into the same equilibrium location, and thus yielding the same steady-state. Moreover, the parameter μ indicates the nonlinearity and the strength of the damping, so increasing μ will shorten the transience up to limit cycle.

Besides Van der Pol oscillator, Dynamic Eigenvalue approach as pointed out above is able to synthesize infinitely many dynamics that generates limit-cycle with modulated frequencies in a real-time fashion. In our design, the frequency synthesizer is fulfilled by series of Van der Pol oscillator with a first-order low-pass filter to shape outputs into a sinusoidal function even when μ is super large for ultra short transience.

Accordingly, the frequency synthesizer is the Van der Pol dynamics:

$$\ddot{z} + \omega^2 z = u$$
$$u = -\mu(z^2 - \frac{a^2}{4})\dot{z}\ ,$$

which has been represented by internal feedback-interconnection, in series with the first-order filter:

$$\tau\dot{y} + y = \sqrt{2}z\ \ (\tau = 1/\omega)\,.$$

By choosing three state variables: $x_1 = z$, $x_2 = \dot{z}$, and $x_3 = y$, the state-space realization of this limit-cycle generator becomes

$$u = -\mu(x_1^2 - \frac{a^2}{4})x_2$$

$$\begin{bmatrix}\dot{x}_1\\ \dot{x}_2\\ \dot{x}_3\end{bmatrix}=\begin{bmatrix}0 & 1 & 0\\ -\omega^2 & 0 & 0\\ \sqrt{2}\omega & 0 & -\omega\end{bmatrix}\begin{bmatrix}x_1\\ x_2\\ x_3\end{bmatrix}+\begin{bmatrix}0\\ 1\\ 0\end{bmatrix}u \tag{25}$$

$$y=\begin{bmatrix}0 & 0 & 1\end{bmatrix}\begin{bmatrix}x_1\\ x_2\\ x_3\end{bmatrix}$$

It appears as a feedback-interconnected LPV form: $u=f(x;\mu,a)$; $\dot{x}=A(\omega)x+Bu$; $y=Cx$, where the command (angular) frequency ω , amplitude a and converging speed μ constitute the slow-time parameter that will be on-line scheduled in a slow-time fashion.

The frequency synthesizer in Eq. (25) is then implemented into a DSP-embedded microcontroller with the Linear Parameter-varying Matrix Iteration Time-fixed (LPV-MIT) method as follows. Continuous-to-digital conversion of Eq. (25) yields

$$\begin{aligned}u_k &= -f(x_k;\mu_j,a_j)\\ x_{k+1} &= \Phi(\omega_j)x_k+\Gamma(\omega_j)u_k\,,\\ y_k &= Cx_k\end{aligned} \tag{26}$$

where k and j are fast-time and slow-time, respectively indexes, and the system matrices (Φ,Γ) will be on-line calculated in a slow-time fashion since the resonant frequency ω is slow-time updated in practice. Explicitly,

$$\Phi(\omega_j)=e^{A(\omega_j)}\approx\sum_{i=0}^{n}\frac{A^i(\omega_j)T^i}{i!};$$

$$\Gamma(\omega_j)\approx T\sum_{i=1}^{n}\frac{A^{i-1}(\omega_j)T^{i-1}}{i!}\,, \tag{27}$$

where T is the fast-time sampling period that is short enough to make the above Taylor-series expansion engineering accurate even with few terms, say, $n=2$ or 3 as T is 0.001 second.

At the present time t_k the DSP controller merely stores the current state x_k , and the update of state from x_k to x_{k+1} at next instant is fulfilled by DSP engine performing the addition and multiplication of floating numbers according to Eq. (26). In the sense, any time can be treated as the initial time, which makes real-time processing best efficient. Moreover, the intervals of state update are held identical to those in computer simulation, so that the real-timed operation matches the dynamics that has been verified by offline calculation, thus achieving robust implementation. At any instances, pulse-width modular (PWM) signal in line with the output y is sent to the gate-driving circuit of switched power converters that drive the sun-to-heatflux actuator in Fig. 1.

Fig. 4 and Fig. 5 visualize the capability of such a DSP-based frequency synthesizer. As shown in Fig. 4, a first-order low-pass filter with right bandwidth shapes the outputs of Van der Pol to be purely sinusoidal, even when the converging parameter μ exceeds requirements. Fig. 5 tests on-line modulation of frequency when the converging parameter μ is large enough. It is really in a real-time fashion, since the DSP scheme according to Eqs (25)-(26) is in the sense that Clock can be reset to zero at any time, as mentioned above.

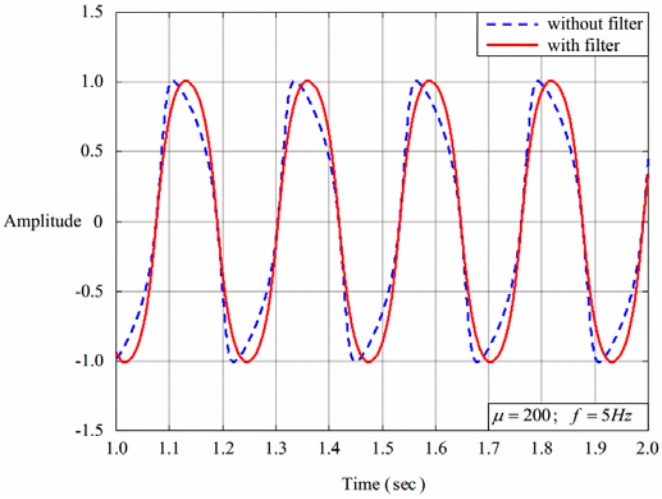

Fig. 4. Shaping Van der Pol oscillator output with first-order filtering.

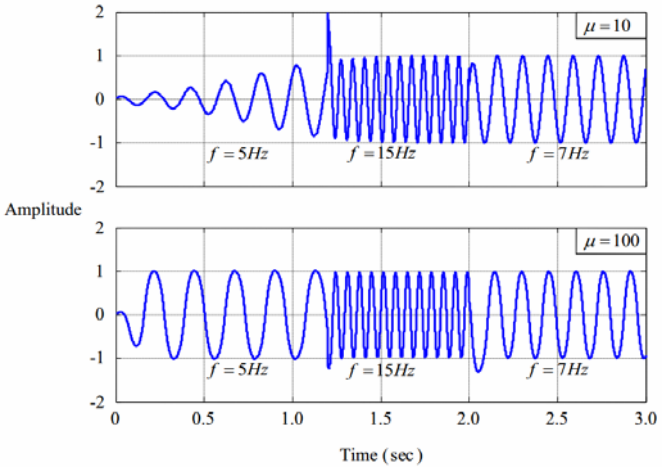

Fig. 5. Online modulation of frequency with filtered Van der Pol oscillator.

5. PROTOTYPING INVESTIGATION

As an demonstration, let the resonant thermoacoustic solar AC power generator is of heat-flux excitation $q=500\ W/m^2$, length of chamber $\ell=3\ m$, cross-section areas of head end and load end $A_0=7m^2$ and $A_\ell=0.7m^2$, respectively, leakage factor $\beta=0.9$, and working temperature $T=300K$ in average. The mechatronic load is closed to be of inertia of 10 kg series-connected by the damping of $4\,nt\cdot\sec/m$.

Fig. 6 and Fig. 7 record the responses of piston stroke and power rating, respectively, as the photo valve is switched at the zero, first, second and third -mode frequencies and the area-ratio A_0/A_ℓ is set from 1 to 10. Fig. 6 shows that the

piston stroke is boosted by increasing the area-ratio A_0/A_ℓ. For example, at first-mode resonance, the piston stroke d_s is boosted from 0.12 cm to 16.75 cm as the area-ratio A_0/A_ℓ is changed from 1 to 10. Due to the boundary friction arising from flow leakage, resonance at higher frequencies yields shorter piston-stokes with a specified area-ratio. As a result, the area-ratio in thermoacoustic engine plays analogously as gear-ratio in power-train transmission to regulate force-velocity.

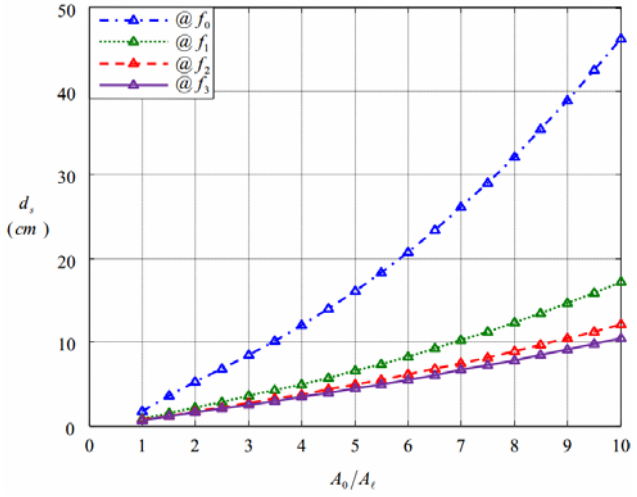

Fig. 6. Piston strokes at resonant frequencies.

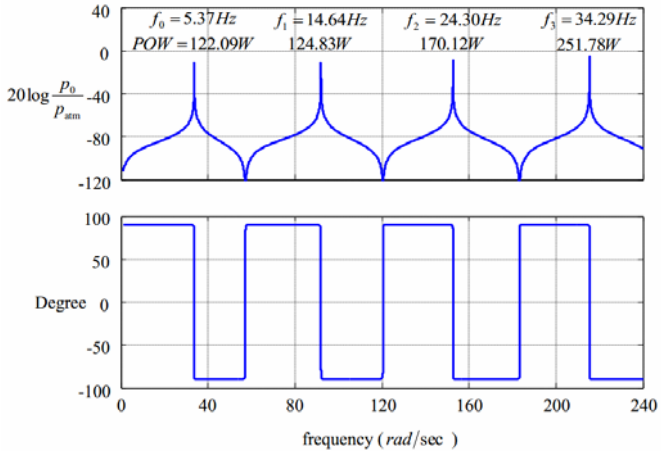

Fig. 7. Power Rating Assessment.

Fig. 7 contains the Bode plot of p_0/p_{atm}, which shows the amplitude of head pressure p_0 and its phase difference θ between the head velocity u_0, across the span of working frequencies. The effect of resonance on power rating can be easily examined by this Bode plot. In the magnitude plot, four resonant frequencies are marked: $f_0 = 5.37Hz$ $f_1 = 14.64Hz$, $f_2 = 24.30Hz$ and $f_3 = 34.29Hz$, at each of which the real power generated by sunlight is marked above each peaks. Therein, known from AC power,

$$POW = U_0 P_0 \cos\theta,$$

where U_0 and P_0 are root-mean-square values of u_0 and p_0, respectively. Generally, the power rating is getting larger along with resonance at higher frequencies, but the piston stroke is getting shorter.

Suppose that the head area is $A_0 = 7m^2$ and the efficiency of electricity generation is 60%, resonant control working at the second-mode frequency can harvest $102.07W$. A suburban family needs almost $1.0KW$ to constant power it up. For any homes possessing more than $70m^2$ rooftop or land spaces, the resonant thermoacoustic engine under investigation is the best candidate served for solar energy generation to power them up or turns electricity meters backward.

6. SUMMARY

This paper develops the disciplines in designing resonance-controlled thermoacoustic AC engines, including analytic Rayleigh dynamics and DSP-based limit-cycle generators. We find that power rating can be remarkably amplified through resonant control of boundary heat-flux as well as efficiency of power transmission can be tremendously increased by shaping the Rijke tube. An investigation on the prototype shows that any homes possessing more than $70m^2$ rooftop spaces can build this rooftop power plant to constant power them up. The above design is unattainable without the following theoretical developments in advance:

(1) DSP-based limit-cycle generators with online adjustable frequencies for amplification of power ratings;

(2) Analytic Rayleigh Dynamics to shape the Rijke tube for efficiency of power transmission;

(3) 2D transfer-function modelling to transform the overall design into feedback systems for optimizing impedance matching of Rijke tube and AC power generator; and

(4) Conservation law of Rayleigh storage to Figure out engine cycles and identify flow leakage.

REFERENCES

Culick, F.E.C. (1987). A note on Rayleigh's criterion. *Combustion Science and Technology*, 56(4-6), 159-166.

de Caro, D., Napoli, E., and Strollo, A.G.M. (2004). Direct digital frequency synthesizers with polynomial hyperfolding technique. *IEEE Transactions on Circuits and Systems-II: Express Briefs*, 51(7), 337-344.

Durox, D., Schuller, T., Noiray, N., Birbaud, A.L., and Candel, S. (2009). Rayleigh criterion and acoustic energy balance in unconfined self-sustained oscillating flames. *Combustion and Flame*, 156(1), 106-119.

Ferreira, M.A. and Carvalho, Jr. J.A. (1997). A simple derivation of the Rayleigh criterion in integral form. *Journal of Sound and Vibration*, 203(5), 889-893.

Hong, B.-S. (2010). Construction of 2D isomorphism for 2D H_∞-control of Sturm-Liouville systems. *Asian Journal of Control*, 12(2),187-199.

Hong, B.-S., Chou, C.-Y., and Lin, T.-Y. (2013). 2D transfer function modelling of thermoacoustic vibration engines

with boundary heat-flux control. *Asian Journal of Control*, 15(6), 1666-1676.

Hong, B.-S. and Lin, T.-Y. (2007). Robust observer designs for thermoacoustic dynamics with distributed-delay heat input. *Asian Journal of Control*, 9(3), 326-332.

Hong B.-S., Lin, T.-Y., and Su, W.-J. (2009) Electric bikes energy management- game-theoretic synthesis and implementation. In *Proceedings of the IEEE International Symposium on Industrial Electronics* (pp. 2131-2136).

Hong, B.-S., Ray, A., and Yang, V. (2002). Wide-range robust control of combustion instability. *Combustion and Flame*, 128(3), 242-258.

Hong, B.-S., Su, P.-J., Chou, C.-Y., and Hung, C.-I. (2011). Realization of non-Fourier phenomena in heat transfer with 2D transfer function. *Applied Mathematical Modelling*, 35(8), 4031-4043.

Jung, S. and Matveev, K.I. (2010). Study of a small-scale standing-wave thermoacoustic engine. *Proceedings of the Institution of Mechanical Engineers, Part C: Journal of Mechanical Engineering Science*, 224(1), 133-141.

Madheswaran, M., and Menakadevi, T. (2003). An improved direct digital synthesizer using hybrid wave pipelining and CORDIC algorithm for software defined radio. *Circuits, Systems, and signal Processing*, 32(3), 1219-1238.

Matveev, K.I. and Culick, F.E.C. (2003). A study of the transition to instability in a Rijke tube with axial temperature gradient. *Journal of Sound and Vibration*, 264(3), 689-706.

Matveev, K.I. and Jung, S. (2011). Modeling of thermoacoustic resonators with nonuniform medium and boundary conditions. *Journal of Vibration and Acoustics*, 133(3), 031012.

Nicoud, F. and Poinsot, T. (2005). Thermoacoustic instabilities: Should the Rayleigh criterion be extended to include entropy changes?. *Combustion and Flame*, 142(1-2), 153-159.

O'Leary, P., and Maloberti, F. (1991). A direct-digital synthesizer with improved spectral performance. *IEEE Transactions on Communications*, 39(7), 1046-1048.

Rabenstein, R. (1999). Transfer function models for multidimensional systems with bounded spatial domains. *Mathematical and Computer Modelling of Dynamical Systems*, 5(3), 259-278.

Rabenstein, R. and Trautmann, L. (2002). Multidimensional transfer function models. *IEEE Transactions on Circuits and Systems I: Fundamental Theory and Applications*, 49(6), 852-861

Rabenstein, R. and Trautmann, L. (2003). Digital sound synthesis of string instruments with the functional transformation method. *Signal Processing*, 83(8), 1673-1688.

Shen, C., He, Y., Li, Y., Ke, H., Zhang, D., and Liu Y. (2009). Performance of solar powered thermoacoustic engine at different tilted angles. *Applied Thermal Engineering*, 29(13), 2745-2756.

Smoker, J., Nouh, M., Aldraihem, O., and Baz, A. (2012). Energy harvesting from a standing wave thermoacoustic-piezoelectric resonator. *Journal of Applied Physics*, 111(10), 104901.

Sujith, E.I., Waldherr, G.A., and Zinn, B.T. (1995). An exact solution for one-dimensional acoustic fields in ducts with an axial temperature gradient. *Journal of Sound and Vibration*,184(3), 389-402.

Tassart, S. (2013). Band-Limited Impulse Train Generation Using Sampled Infinite Impulse Responses of Analogue Filters. *IEEE Transactions on Audio, Speech, and Language Processing*, 21(3), 488-497.

Vankka, J., Waltari, M., Kosunen, M., and Halonen, K.A.I. (1998). A direct digital synthesizer with an on-chip D/A-converter. *IEEE Journal of Solid-State Circuits*, 33(2), 218-227.

Wang, G., Yang. R., and Xu, D. (2013). DSP-based control of sensorless IPMSM drives for wide-speed range operation. *IEEE Transactions on Industrial Electronics*, 60(2), 720-727.

Wu, Z., Dai, W., Man, M., and Luo, E. (2012). A solar-powered traveling-wave thermoacoustic electricity generator. *Sol Energy*, 86(9), 2376-2382.

Yang, B.-D., Choi, J.-H., Han, S.-H., Kim, L.-S., and Yu, H.-K. (2004). An 800-MHz low-power direct digital frequency synthesizer with an on-chip D/A converter. *IEEE Journal of Solid-State Circuits*, 39(5), 761-774.

Yeary, M.B., Fink, R.J., Beck, D., Guidry, D.W., and Burns, M. (2004). A DSP-based mixed-signal waveform generator. *IEEE Transations on Instrumentation and Measurement*, 53(3), 663-671.

Yeoh, H.-C., Jung, J.-H., Jung, Y.-H., and Baek, K.-H. (2010). A 1.3-GHz 350-mW hybrid direct digital frequency synthesizer in 90-nm CMOS. *IEEE Journal of Solid-State Circuits*, 45(9), 1845-1855.

Yu, Z. and Jaworski, A.J. (2010). Impact of acoustic impedance and flow resistance on the power output capacity of the regenerators in travelling-wave thermoacoustic engines. *Energy Conversion and Management*, 51(2), 350-359.

Yu, Z., Jaworski, A.J., and Backhaus, S. (2012). Travelling-wave thermoacoustic electricity generator using an ultra-compliant alternator for utilization of low-grade thermal energy. *Applied Energy,* 99, 135-145.

Zhao, D. (2012). Transient growth of flow disturbances in triggering a Rijke tube combustion instability. *Combustion and Flame*, 159(6), 2126-2137.

Zhao, D. (2013). Waste thermal energy harvesting from a convection-driven Rijke-Zhao thermo-acoustic-piezo system. *Energy Conversion and Management*, 66, 87-97.

Zhao, D. and Chew, Y. (2012). Energy harvesting from a convection-driven Rijke-Zhao thermoacoustic engine. *Journal of Applied Physics*, 112, 114507.